13th International Conference on
Structural Health Monitoring of Intelligent Infrastructure
DOI: 10.3217/978-3-99161-057-1-070

Integrated Motion Measurement – a Tool for Structural Health Monitoring?

M. Kohl[1, 0009-0000-6512-6219], J. F. Wagner[1, 0000-0002-8536-4668]
[1]Chair of Flight Measuring Technology, University of Stuttgart, Pfaffenwaldring 31, 70569 Stuttgart, Germany
email: michael.kohl@pas.uni-stuttgart.de, jfw@pas.uni-stuttgart.de

ABSTRACT: Integrated Motion Measurement Systems (IMMSs) are multi-sensor systems, based on the principle of integrated navigation with inertial sensors as central components and an aiding by, e.g., GNSS receivers. IMMSs can be used to track elastic motions as additional degrees of freedom (DOFs) that capture the deformations of the object. To support the estimation of elastic properties, additional internal aiding measurements like strain gauges can be implemented. In addition to the raw sensor data, the elastic DOFs in the time and frequency domain are possible indicators to be used for Structural Health Monitoring (SHM).

With the increasing availability of low-cost micro-electro-mechanical systems (MEMSs), combined with their ease of implementation, applications in large sensor quantities become feasible. To validate and experimentally test such an integrated motion measurement, a test rig with a movable, flexible pendulum beam was designed, to represent an idealization of a mast, rotor blade, or aircraft wing.

In this study a short categorization of possible SHM applications for IMMSs is given, based on previous work and state-of-the-art SHM approaches. In this context, the principle of IMMS is explained with the experimental realization, validation, and the resulting modal characteristics of the elastic DOFs as potential indicators for SHM. Furthermore, the importance of strain gauges is investigated with methods to reduce their number by redundant sensors and restricted aiding.

KEY WORDS: Sensor fusion; Kalman filter; Inertial sensors; Complementary Sensors.

1 INTRODUCTION

Integrated motion measurement of flexible structures is the expansion of conventional integrated navigation systems, typically employing an inertial measurement unit (IMU) aided by GNSS (global navigation satellite system) [1-3]. In contrast to the classic approach, the object of interest is now developed from a simple rigid point with six degrees of freedom (DOFs, three for the position and three for the attitude) to an elastic body with extra DOFs, capturing elastic deformations. Furthermore, additional sensors are distributed on the structure, enabling this model extension. Such additional sensors are, on the one hand, inertial sensors like accelerometers or gyroscopes to expand the system input to accommodate the extra DOFs. On the other hand, further GNSS receivers, strain gauges, or other sensor types are feasible for aiding [4].

With the ongoing development and miniaturization of micro-electromechanical systems (MEMSs), such integrated motion measurement systems (IMMSs) can now be realized with cost-effective sensors. A test rig [5], as well as a hybrid sensor system [6] was developed to validate the principle of IMMS on a flexible beam. The test rig and beam were designed to resemble an aircraft wing, mast, or rotor blade of a wind turbine. The validation proved that such low-cost sensor systems are suitable for IMMS applications and can reliably estimate structural deformations [7]. Concluding, IMMSs for flexible structures allow a comprehensive movement determination of the object including the rigid body part as well as elastic deformation of the structure itself.

The validation [7] so far relied on the usage of a quantity of strain gauges being the same as the number of characteristic deformations introduced as additional DOFs. This means that with rising complexity of the structure and increased number of relevant mode shapes, more strain gauges are needed to complete the system requirements. Despite dominant advantages like high sensitivity leading to a reliable aiding of the selected deformations, certain disadvantages would benefit a reduction of these sensors. Such disadvantages are i.e. a complex installation process as well as maintenance. Installing strain gauges can be a lengthy and complex task that demands skill and accuracy. It requires specialized knowledge to ensure that the gauges are attached, wired, and calibrated correctly. Furthermore, strain gauges are vulnerable to environmental factors and therefore need to be shielded adequately. All these factors can add to the overall complexity of the project [8]. In contrast to that, the application of IMUs and Time-of-Flight distance sensors (ToFs) is relatively easy. In the present setup, both sensors are located on a circuit board and screwed to the structure [6]. It can be beneficial to reduce the usage of strain gauges in favor of low-cost, easy to apply sensors like IMUs, ToFs, or GNSS receivers for installation and maintenance reasons.

The additional estimation of deformations by a distributed sensor network puts IMMSs in the spotlight as a potential application for vibration-based structural health monitoring (SHM) at a global approach. Unlike local methods, where a dense sensor network is setup around a perimeter of expected damage, the behavior of the complete structure is evaluated for damage diagnosis [9]. An abundance of methods exists in this field, however, to the knowledge of the authors, no existing method utilizes the estimation of elastic deformations via kinematic considerations:

DOI: 10.3217/978-3-99161-057-1-070

In state-of-the-art SHM applications, accelerometers are widely used as sensors and typical parameters for damage evaluation are modal parameters like natural frequencies and mode shapes. Often, the input or output signals are further processed by methods like Fast Fourier transform (FFT), or Wavelet transform (WT) [10]. While several methods combine IMU or accelerometer data with GNSS measurements [11-13], the sensor network or node is treated as a rigid body and in practice, the displacement of the monitored location is extracted for signal evaluation. On the other hand, applications with distributed sensors, mostly accelerometers without any aiding exist. For example, a network of low-cost MEMS accelerometers is applied in a bridge structure for displacement and vibration analysis [14]. In this case, modal parameters like frequencies, damping ratios and amplitudes are estimated based on the model of a damped harmonic oscillator. Subsequently, the mode shapes are extracted from the calculated amplitudes of the involved sensor locations and modes. In other applications, the overall deflection of a bridge [15] or wind turbine [16] is reconstructed based on the calculated rotation angles of distributed IMUs or accelerometers, gyroscopes, and magnetometers respectively. The latter method proposes to use the obtained deflection to assess the occurring stresses via a Finite Element (FE) simulation for SHM.

Furthermore, many papers suggest the usage of Operational Modal Analysis (OMA). Here, only the measurement data with unknown system excitation is used to obtain modal parameters of the observed structure. A commercial OMA tool is for example used to identify different damage scenarios of an open-source benchmark system with distributed accelerometers [17]. In other OMA applications, simulated accelerometer data of distributed sensors are used to extract mode shapes [18] or natural frequencies, mode shapes, and curvature mode shapes [19] for floating offshore wind turbines and wind turbine blades respectively. Damage detection can then be applied by assessing the change of mode shape after applying damages [19]. Alternatively, distributed strain sensors in the form of Fiber Bragg Gratings (FBGs) can be used for damage detection by identifying the change of eigenfrequencies, obtained from OMA on a wind turbine structure [20].

In another approach, damage assessment is done by Finite Element Model Updating for a laboratory bridge structure equipped with accelerometers [21]. Based on the measurements obtained, the mass, damping, and stiffness matrices of the FE simulation are updated to match the characteristics of the measurements. To conclude, there exist a variety of SHM methods and applications which could potentially be adapted to an IMMS, which aims at a more complementary, integrated use of different types of sensors.

Thus, in this study, a preliminary classification and outlook on potential SHM applications by IMMS is conducted. Furthermore, the reduction as well as replacement of strain gauges with different sensor types and aiding approaches is investigated. For that, Section 2 introduces the concept of IMMS of flexible structures, including the general system equations and the kinematic equations for accelerometers and gyroscopes as central components. Section 3 provides the application of such a system for a flexible beam, introducing unit deformations as characteristic elastic deformations and aiding models of different sensor types. The test rig for experimental implementation as well as a summary of the conducted validation are presented subsequently. Based on this, the experimental approach of this study is presented in Section 4, followed by the presentation and discussion of the results in Section 5. A conclusion and outlook finalize the paper in Section 6.

2 INTEGRATED MOTION MEASUREMENTS OF FLEXIBLE STRUCTURES

The main task of IMMSs is to track the propagation with time of the motion state vector

$$\mathbf{x}(t) = \begin{bmatrix} \mathbf{r}(t) & \dot{\mathbf{r}}(t) & \boldsymbol{\Theta}(t) & \cdots \end{bmatrix}^{\mathrm{T}}, \tag{1}$$

which holds the classical navigation parameters position $\mathbf{r}$, velocity $\dot{\mathbf{r}}$, and attitude $\boldsymbol{\Theta}$. The state vector is further expanded by additional DOFs reflecting elastic deformations, which will be derived within this section. Other typical parameters like sensor biases are excluded for a better overview [4]. The dynamic behavior of $\mathbf{x}$ can be modelled by a nonlinear, kinematical model

$$\dot{\mathbf{x}} = \mathbf{f}(\mathbf{x}, \mathbf{u}) + \mathbf{G}\mathbf{w}, \tag{2}$$

driven by the input vector $\mathbf{u}(t)$. In the case of IMMSs, the input consists of accelerations and angular rates, measured by an array of inertial sensors. Additionally, the stochastic measurement noise $\mathbf{w}(t)$ of the input is mapped to $\dot{\mathbf{x}}$ via the noise matrix $\mathbf{G}$. Inherent errors like sensor noise and bias of the input $\mathbf{u}$, in combination with numerical integration leads to a rising error if the system state $\mathbf{x}$ is calculated from Equation (2). To reduce this error and ensure observability of the system, regular correcting measurements are necessary which are represented by the aiding vector

$$\mathbf{y} = \mathbf{h}(\mathbf{x}, \mathbf{u}) + \mathbf{v}. \tag{3}$$

The aiding vector $\mathbf{y}(t)$ comprises measurements, e.g. from GNSS receivers, which can be modeled according to the current system state $\mathbf{x}$, input $\mathbf{u}$, and their stochastic measurement noise $\mathbf{v}(t)$ [1].

The IMMS combines the calculated system state from Equation (2) with the aiding Equation (3) to merge different sensor types by using the advantages of each sensor type against the disadvantages of the other sensors. This so-called sensor fusion, as well as solving the differential Equation (2) is accomplished by an extended Kalman Filter (EKF). The system architecture and signal flow of an EKF, which works according to the observer principle, is depicted in Figure 1 [22].

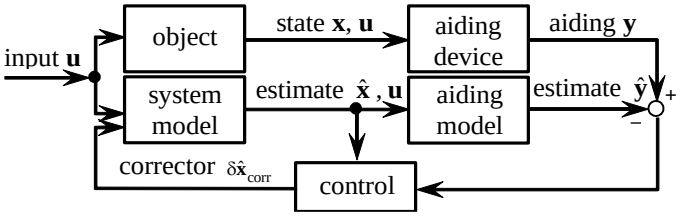

Figure 1. System architecture of IMMS. Adapted from Wagner and Wieneke [22].

The system state $\mathbf{x}$ and therefore the aiding vector $\mathbf{y}$ results from the accelerations and angular rates acting on the object,

DOI: 10.3217/978-3-99161-057-1-070

which are measured by the input $\mathbf{u}$. Based on this input, an estimate of the system state $\hat{\mathbf{x}}$ and measurement vector $\hat{\mathbf{y}}$ is calculated. Conclusively, the difference between actual aiding measurements and their estimation $\mathbf{y}-\hat{\mathbf{y}}$ is used to calculate an updated system state $\hat{\mathbf{x}}$.

2.1 Kinematic system model and input

To complete the state vector from Equation (1), to accommodate elastic deformations, and to give an overview of the involved input sensors within an IMMS, a simplified model of an aircraft fuselage with one wing as a beam is depicted in Figure 2.

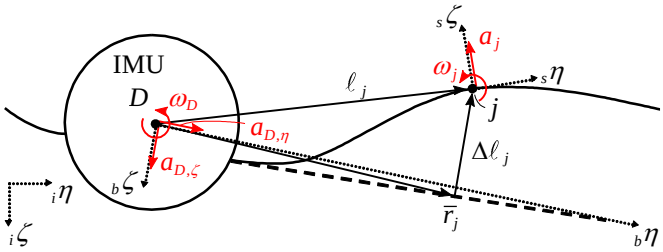

Figure 2. Simplified aircraft model with exemplary input sensors. Adapted from Örtel [4].

The wing is sketched in its deformed (solid line) and undeformed (dashed line) state. In this case, measurements of the input vector $\mathbf{u}$ are indicated as red arrows, which are comprised of the accelerations $a_{D,\eta}, a_{D,\zeta}$, and the angular rate ω_D obtained from an IMU in the center of the system D. Furthermore, additional peripheral accelerometers or gyroscopes at arbitrary positions j measure either the acceleration a_j or angular rate ω_j. Instead of single-axis accelerometers or gyroscopes, complete IMUs can be installed as peripheral sensors, however, only one of the signals shown is mandatory for the presented system model. The relevant coordinate systems are indicated by dotted arrows, which are the inertial coordinate system $({}_i\eta, {}_i\zeta)$, the body coordinate system $({}_b\eta, {}_b\zeta)$, and the sensor coordinate system $({}_s\eta, {}_s\zeta)$. Accelerations and angular rates are measured with respect to the inertial coordinate system, in either the body coordinate system (IMU in the center D) or the sensor coordinate system (peripheral sensor in j). The lever arm ℓ_j is the distance between D and j. In the case of peripheral accelerometers, the kinematic equation of motion of j is

$$ {}^i\ddot{\mathbf{r}}_j = {}^i\ddot{\mathbf{r}}_D + {}^b\ddot{\boldsymbol{\ell}}_j + 2\left(\boldsymbol{\omega}_{bi} \times {}^b\dot{\boldsymbol{\ell}}_j\right) + {}^i\dot{\boldsymbol{\omega}}_{bi} \times \boldsymbol{\ell}_j + \boldsymbol{\omega}_{bi} \times \left(\boldsymbol{\omega}_{bi} \times \boldsymbol{\ell}_j\right), \quad (4) $$

with ${}^i\ddot{\mathbf{r}}_j$ comprising a_j, which is therefore directly measured by the peripheral accelerometer (the left superscript indicates the reference system for differentiation). Furthermore, ${}^i\ddot{\mathbf{r}}_D$ holds the accelerations $a_{D,\eta}, a_{D,\zeta}$, whereas $\boldsymbol{\omega}_{bi}$ contains the angular rate ω_D, meaning both vectors are readily available from the IMU measurements in D. With lack of low-cost angular acceleration sensors, $\dot{\boldsymbol{\omega}}_{bi}$ is calculated via numerical differentiation of $\boldsymbol{\omega}_{bi}$. Considering peripheral gyroscopes, the kinematic equation of motion becomes

$$ \boldsymbol{\omega}_j = \boldsymbol{\omega}_{bi} + \frac{\mathrm{d}\left(\mathrm{rot}\,\boldsymbol{\ell}_j\right)}{\mathrm{d}t}. \quad (5) $$

Here, $\boldsymbol{\omega}_j$ is directly measured by the peripheral gyroscope with ω_j. Both Equations (4) and (5) contain the unknown lever arm $\boldsymbol{\ell}_j$ and its first and second derivative (${}^b\dot{\boldsymbol{\ell}}_j$ and ${}^b\ddot{\boldsymbol{\ell}}_j$) in the case of peripheral accelerometers [4].

As indicated in Figure 2, the lever arm $\boldsymbol{\ell}_j$ is modeled by a rigid part $\bar{\mathbf{r}}_j$ on the undeformed wing plus a time-dependent, elastic part $\Delta\boldsymbol{\ell}_j(t)$. Under the assumption of small deformations, the lever arm is modeled by a series approach

$$ \boldsymbol{\ell}_j = \bar{\mathbf{r}}_j + \Delta\boldsymbol{\ell}_j(t) \approx \bar{\mathbf{r}}_j + \sum_{\chi=1}^{\Gamma}\left(b_\chi(t)\cdot\mathbf{s}_\chi(\bar{\mathbf{r}}_j)\right), \quad (6) $$

with a selected number Γ of time-dependent deformation variables $b_\chi(t)$ as a coefficient to their associated shape functions $\mathbf{s}_\chi(\bar{\mathbf{r}}_j)$. The deformation variables act as additional DOFs and reflect the current amplitudes of the shape functions, which spatially represent the structural deformations. For the latter, it is assumed that $\mathbf{s}_\chi(\bar{\mathbf{r}}_j)$ only have components in ${}_b\zeta$-direction, which justifies the usage of single-axis sensors (more components require more sensor-axes). Additionally, the shape functions are defined in a way that they have the maximum displacement value of 1 at least at one point. Due to this definition, they will be referred to as unit deformations, of which two exemplary selections $\mathbf{s}_1(\bar{\mathbf{r}}_j)$ and $\mathbf{s}_2(\bar{\mathbf{r}}_j)$ are sketched in Figure 3. In this case the rigid part $\bar{\mathbf{r}}_j$ of the lever arm is aligned with the η-axis of the body coordinate system.

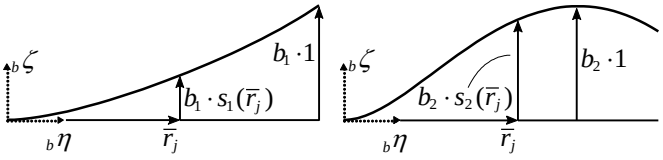

Figure 3. Typical unit deformations. Adapted from Örtel [4].

As a result, the superposition of all selected unit deformations multiplied with their current amplitudes should reflect the total deformation of the structure. Consequently, the choice of type and number of unit deformations is essential for a proper approximation of the structure. It has been proven that the eigenmode shapes are a reasonable, but not mandatory choice for the unit deformations [4,7].

Based on Equation (6), the first and second derivative of $\boldsymbol{\ell}_j$ can be formulated with

$$ \begin{aligned} {}^b\dot{\boldsymbol{\ell}}_j &= \sum_{\chi=1}^{\Gamma}\left(\dot{b}_\chi(t)\cdot\mathbf{s}_\chi(\bar{\mathbf{r}}_j)\right) \\ {}^b\ddot{\boldsymbol{\ell}}_j &= \sum_{\chi=1}^{\Gamma}\left(\ddot{b}_\chi(t)\cdot\mathbf{s}_\chi(\bar{\mathbf{r}}_j)\right) \end{aligned}. \quad (7) $$

With the abbreviation $\mathbf{s}_\chi(\bar{\mathbf{r}}_j) = \mathbf{s}_{\chi,j}$, Equations (7) are substituted into (4), to deliver the set of Equations

$$ \begin{aligned} \ddot{b}_\chi(t) = f\big(& {}^i\ddot{\mathbf{r}}_1,\ldots,{}^i\ddot{\mathbf{r}}_\nu,\ldots,{}^i\ddot{\mathbf{r}}_D,\boldsymbol{\omega}_{bi}, \\ & \dot{b}_1,\ldots,\dot{b}_\Gamma,b_1,\ldots,b_\Gamma,\mathbf{s}_{1,1},\ldots,\mathbf{s}_{\Gamma,\nu}\big), \end{aligned} \quad (8) $$

for $\chi = 1,\ldots,\Gamma$ selected unit deformations and $j = 1,\ldots,\nu$ peripheral accelerometers. Substituting Equation (6) into (5) yields

$$ \dot{b}_\chi(t) = f\left(\boldsymbol{\omega}_1,\ldots,\boldsymbol{\omega}_\nu,\boldsymbol{\omega}_{bi},\mathrm{rot}\,\mathbf{s}_{1,1},\ldots,\mathrm{rot}\,\mathbf{s}_{\Gamma,\nu}\right), \quad (9) $$

for $\chi = 1,\ldots,\Gamma$ selected unit deformations and $j = 1,\ldots,\nu$ peripheral gyroscopes [4].

DOI: 10.3217/978-3-99161-057-1-070

Depending on the type of peripheral sensor being either accelerometer (acc) or gyroscope (gyro), the state vector from Equation (1) becomes

$$\mathbf{x}_{\text{acc}} = \left[{}_i\mathbf{r}_D \quad {}_i\dot{\mathbf{r}}_D \quad \boldsymbol{\Theta} \quad \mathbf{b} \quad \dot{\mathbf{b}} \right]^{\mathrm{T}} \quad \text{or} \quad \mathbf{x}_{\text{gyro}} = \left[{}_i\mathbf{r}_D \quad {}_i\dot{\mathbf{r}}_D \quad \boldsymbol{\Theta} \quad \mathbf{b} \right]^{\mathrm{T}}, \tag{10}$$

according to the general form of Equation (2). All selected deformation variables $b_1,\ldots,b_\Gamma$ and their derivatives are summarized in the vectors $\mathbf{b}$ and $\dot{\mathbf{b}}$ respectively. The system input becomes

$$\mathbf{u}_{\text{acc}} = \left[a_{D,\eta} \quad a_{D,\zeta} \quad \omega_D \quad \dot{\omega}_D \quad \mathbf{a} \right]^{\mathrm{T}} \quad \text{or} \quad \mathbf{u}_{\text{gyro}} = \left[a_{D,\eta} \quad a_{D,\zeta} \quad \omega_D \quad \boldsymbol{\omega} \right]^{\mathrm{T}}, \tag{11}$$

with $\mathbf{a}$ and $\boldsymbol{\omega}$ holding all measured peripheral accelerations $a_1,\ldots,a_\nu$ and angular rates $\omega_1,\ldots,\omega_\nu$. To maintain the observability of the IMMS, the number of peripheral sensors must be equal or higher than the elastic DOFs $\nu \geq \Gamma$. A further condition is that the chosen unit deformations need to be linear independent, and the sensor positions must be chosen adequately [4].

2.2 Aiding equations and measurements

The aiding Equation (3) relates the actual aiding measurements $\mathbf{y}$ to their estimate $\hat{\mathbf{y}}$, to correct the state estimate $\hat{\mathbf{x}}$ according to Figure 1. To achieve that, the measurements need to be reconstructed from the system state, which corresponds to the right-hand side of Equation (3). Aiding equations can be divided into two principles, with applications in Section 3:

External aiding: The systems providing the measurements are independent and located outside of the object. A prominent example of such an aiding system are GNSSs. If the system, i.e. provides a position or distance reference of a point *j*, the measurement can be related with a function including the position, orientation, and the deformations [4].

Internal aiding: The measurement systems are located on the structure. Strain gauges, for example, provide data which can be related to the elastic DOFs only [4].

3 IMMS APPLICATION OF A FLEXIBLE BEAM

For experimental validation and application of IMMS of flexible structures, the simplified aircraft model from Figure 2 was reduced to a suspended, elastic pendulum as shown in Figure 4. This setup should abstract the aircraft fuselage and one wing as the pendulum bearing *D* and the pendulum itself. This representation also holds for a rotor or mast of a wind turbine and is therefore generally applicable. Considering technical limitations and the desired realization, all inertial sensors are applied in the form of a six-axis IMU measuring three accelerations and three angular rates. This means, that an IMU is placed in *D*, measuring $a_{D,\eta}$, $a_{D,\zeta}$, and ω_D, as well as in j_s, measuring a_{js} and ω_{js}. As a result of restricted GNSS visibility due to an indoor test rig, Time-of-Flight distance sensors (ToFs) are placed alongside the peripheral IMUs, measuring the distance ρ_j from the point j_ρ towards a reflector plane, placed at the known location d_{ref}. Internal aiding is provided via strain gauges, which are applied as a wheatstone full bridge, measuring the bending strain ε_j in the location j_ε close to the IMU. The setup is completed by a high precision distance sensor, providing the displacement of the bearing ρ_D. The Pendulum is a steel sheet of the material DX51D+Z, with the dimension 4 m x 0.2 m x 0.002 m [5,7].

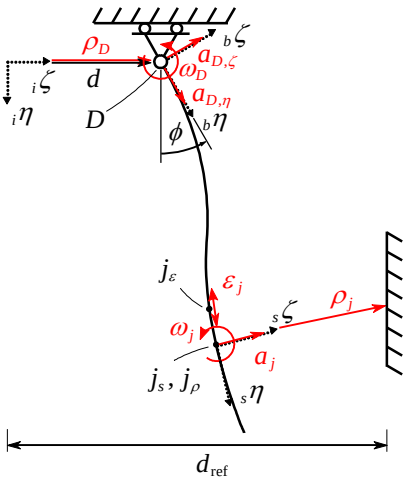

Figure 4. Experimental IMMS setup [7].

The state vector of the IMMS can be taken directly from Equation (10), with

$${}_i\mathbf{r}_D = \left[d \quad h \right]^{\mathrm{T}}, \boldsymbol{\Theta} = \phi \tag{12}$$

and h being the displacement of D in ${}_i\eta$-direction. The input follows from Equation (11) without adjustments, including $j_s = 1,\ldots,\nu_s$ peripheral accelerometers or gyroscopes. Ultimately, the aiding vector becomes

$$\mathbf{y}_{\text{acc}} = \mathbf{y}_{\text{gyro}} = \left[\boldsymbol{\rho}_D \quad \dot{\boldsymbol{\rho}}_D \quad \boldsymbol{\rho} \quad \boldsymbol{\varepsilon} \right]^{\mathrm{T}}. \tag{13}$$

The vectors $\boldsymbol{\rho}$ and $\boldsymbol{\varepsilon}$ hold the data set of all measured distances $\rho_1,\ldots,\rho_\nu$ and bending strains $\varepsilon_1,\ldots,\varepsilon_\nu$ from $j_\rho = 1,\ldots,\nu_\rho$ utilized ToFs and $j_\varepsilon = 1,\ldots,\nu_\varepsilon$ strain gauges. The position measurement $\boldsymbol{\rho}_D$ contains the horizontal distance of the bearing ρ_D corresponding to d and a pseudo-measurement of 0 corresponding to h respectively. In the final application, not all available sensor signals are utilized, meaning that an IMU is used without the accompanying ToF or vice versa. Therefore a distinction between placement and number of the sensors at hand ν_s, ν_ρ, and ν_ε must be made.

3.1 Unit deformations

The unit deformations of the pendulum are acquired from the eigenmodes of the linearized structure. These were calculated with a Finite Element (FE) analysis in ANSYS®. As indicated in Figure 2 and 3, the unit deformations are relevant from the perspective of the object and therefore should be transformed into body coordinates. The first six transformed modeshapes are plotted in Figure 5, where the first two modes of the structure have similar shape due to the transformation. As a result, these two modes are merged to a combimode, since their distinction by the system can not be guaranteed [4,7].

Consequently, the first six modeshapes are represented by the first five unit deformations $\Gamma = 1,\ldots,5$, with the third mode corresponding to the second unit deformation, etc. The eigenfrequencies as well as the associated modes of each unit deformation are listed in Table 1.

DOI: 10.3217/978-3-99161-057-1-070

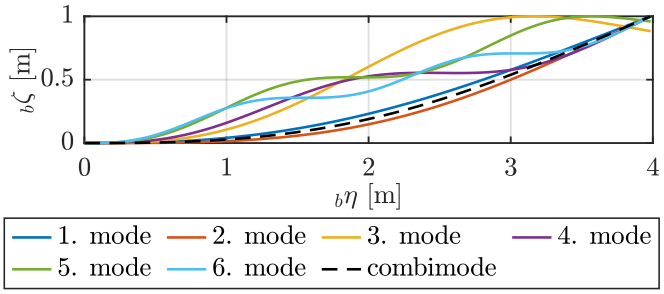

Figure 5. First six transformed modeshapes [4,7].

Table 1. Allocation of eigenmodes to unit deformations with corresponding frequencies [7].

Unit def.	1		2	3	4	5
mode	1	2	3	4	5	6
f_i [Hz]	0.302	0.860	1.909	3.492	5.262	8.318

3.2 Beam deflection, curvature, and aiding equations

To give insight into the applied aiding measurements and equations, a sketch of the randomly deformed pendulum is shown in Figure 6. Furthermore, an arbitrary point (or sensor) *j*, placed at position ℓ_j on the undeformed wing with deformation $\Delta\ell_j$ is highlighted. The sensor coordinate system *s* is rotated relative to the body system *b* by the angle $\phi_{j,sb}$, whereas *b* is rotated by ϕ relative to the inertial system *i*.

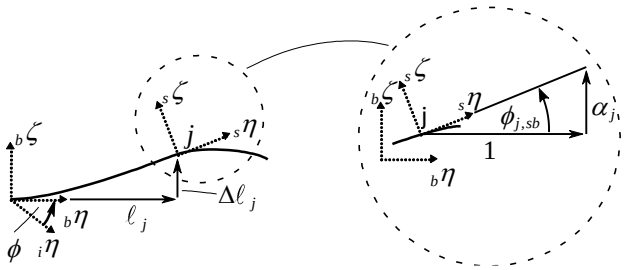

Figure 6. Relation between the local rotation and gradient of the bending line.

Considering $j = 1,\ldots,\nu$ arbitrary peripheral points, the elastic deformation of the object at each location can be reconstructed with

$$\begin{bmatrix}\Delta\ell_1\\ \vdots\\ \Delta\ell_\nu\end{bmatrix} = \begin{bmatrix}s_{1,1} & \cdots & s_{\Gamma,1}\\ \vdots & \ddots & \vdots\\ s_{1,\nu} & \cdots & s_{\Gamma,\nu}\end{bmatrix}\cdot\begin{bmatrix}b_1\\ \vdots\\ b_\Gamma\end{bmatrix} = \mathbf{S}\cdot\mathbf{b} \tag{14}$$

and the matrix of unit deformations $\mathbf{S}$. With the angle ϕ being permanently calculated as part of the state vector, the location of j in the inertial coordinate system is given by the transformation

$${}_i\mathbf{r}_j = \begin{bmatrix}{}_i\eta_j\\ {}_i\zeta_j - d\end{bmatrix} = \begin{bmatrix}\cos\phi & -\sin\phi\\ \sin\phi & \cos\phi\end{bmatrix}\cdot\begin{bmatrix}\ell_j\\ \Delta\ell_j\end{bmatrix} \tag{15}$$

for small deformations. Under the same condition, the rotation $\phi_{j,sb}$ from the body to the sensor coordinate system can be approximated by the gradient of the bending line α_j. Considering the rotation of *b* relative to *i*, the total rotation of *s* relative to *i* can be formulated with

$$\begin{bmatrix}\phi_1\\ \vdots\\ \phi_\nu\end{bmatrix} \approx \phi + \begin{bmatrix}\alpha_1\\ \vdots\\ \alpha_\nu\end{bmatrix} = \phi + \begin{bmatrix}s'_{1,1} & \cdots & s'_{\Gamma,1}\\ \vdots & \ddots & \vdots\\ s'_{1,\nu} & \cdots & s'_{\Gamma,\nu}\end{bmatrix}\cdot\begin{bmatrix}b_1\\ \vdots\\ b_\Gamma\end{bmatrix} = \phi + \mathbf{S}'\cdot\mathbf{b} \tag{16}$$

and

$$\frac{\partial s_{\chi,j}}{\partial\,{}_b\eta} = s'_{\chi j} \tag{17}$$

being the gradient of the unit deformations [4].

While the aiding measurements $\boldsymbol{\rho}_D$ and $\dot{\boldsymbol{\rho}}_D$ directly correspond to the system states $\mathbf{r}_D$ and $\dot{\mathbf{r}}_D$, the remaining aiding measurements have to be viewed in detail:

ToFs: The distance ρ_j is measured perpendicular to the local sensor position as sketched in Figure 7. With the location of the sensor, calculated from Equation (15), and the rotation ϕ_j from Equation (16), the distance measurement can be modeled by the function

$$\rho_j = \frac{d_{\text{ref}} - {}_i\zeta_j}{\cos\phi_j} = h(d,\phi,\mathbf{b})\,. \tag{18}$$

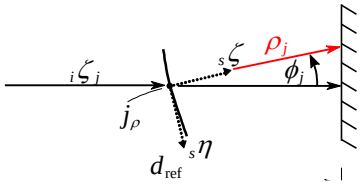

Figure 7. Distance measurement of peripheral ToF sensor.

Strain gauges: Considering the area moment of inertia and the moment of resistance, the bending strain of a rectangular beam of thickness $h*$ can be expressed for small deflections with

$$\begin{bmatrix}\varepsilon_1\\ \vdots\\ \varepsilon_\nu\end{bmatrix} = -\frac{h*}{2}\begin{bmatrix}s''_{1,1} & \cdots & s''_{\Gamma,1}\\ \vdots & \ddots & \vdots\\ s''_{1,\nu} & \cdots & s''_{\Gamma,\nu}\end{bmatrix}\cdot\begin{bmatrix}b_1\\ \vdots\\ b_\Gamma\end{bmatrix} = \mathbf{S}''_\varepsilon\cdot\mathbf{b} = \mathbf{h(b)} \tag{19}$$

for ν_ε applied strain gauges.

3.3 Test rig

The implementation of the IMMS setup from Figure 4 is implemented by a test rig shown in the big picture of Figure 8. The movable pendulum 1 is suspended with a plain bearing 2 from a guidance rail 3. A reflector plane 4 for the ToFs completes the general structure. To impose movements *d* on the pendulum, a linear spindle actuator is mounted underneath the guidance rail and connected to the bearing suspension. The reproducible excitation of the system can then be used to provide comparability between different measurements and input for simulations [5].

The intended input and aiding measurements of Equations (11) and (13) are realized by a hybrid sensor system [6], developed for this application. The system consists of multiple interconnected printed circuit boards (PCBs) as shown in the small picture of Figure 8, which accommodate an IMU, a ToF, along with an analogue to digital converter (ADC) to connect the strain gauges. An additional PCB reads the measurements of the displacement sensor in the bearing. Controlled by a Master PCB, the measurement system provides simultaneous

DOI: 10.3217/978-3-99161-057-1-070

measurements of the implemented sensor types at multiple, selectable positions.

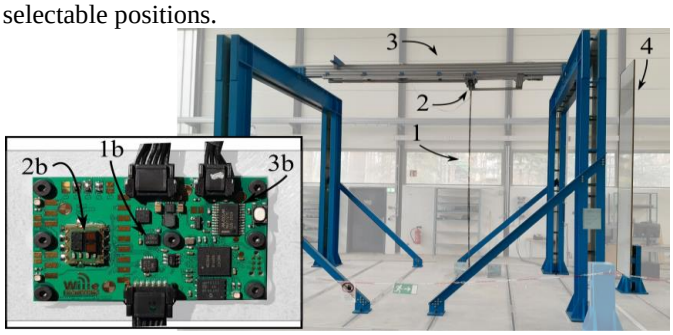

Figure 8. Test rig (big picture) and PCB (small picture) with IMU 1b, ToF 2b and ADC 3b [5].

3.4 *Validation results*

For validation, a practicable and realistic displacement function for the actuator was created. The displacement consists of back-and-forth movements, superimposed by frequency components up to the fifth eigenfrequency of Table 1. The resulting displacement $d(t)$ is plotted in Figure 9, including an initial resting phase of 60 s for initialization purposes. As comparison parameters, the horizontal displacement d of the bearing, the angular orientation ϕ, and the pseudo-elastic deformation e were chosen, the latter being the joint-related deformation and calculated by $\Delta\ell$ according to Equation (14) at the lower tip of the pendulum. To evaluate the IMMS, the FE model from Section 3.1 was simulated with the displacement input measured by ρ_D. To create a realistic scenario, an artificial white noise is added to ρ_D, which is in the order of magnitude of the sensor noise of the ToFs.

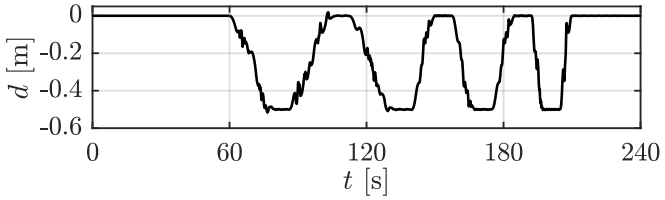

Figure 9. Displacement function $d(t)$ [7].

It could be proven that for this excitation, the errors of attitude $\Delta\phi$ and pseudo-elastic deformation Δe converge with four involved unit-deformations $\Gamma = 4$ and four peripheral sensors (accelerometers or gyroscopes) $\nu_s = \nu_\rho = \nu_\varepsilon = 4$. The position error Δd was insignificantly affected by the inclusion of the elastic DOFs. A comparison of the attitude ϕ and pseudo-elastic deformation e is shown in Figure 10 for a time interval with relatively high dynamics. The simulated parameters (sim) are compared against the accelerometer (acc) and gyroscope (gyro) configuration of the converged case.

Despite time intervals with high dynamics, resulting in large deflections and other nonlinear effects, the results indicated that the IMMS delivers reliable estimates of the classical navigation parameters and the elastic deformation. A clear difference between the two sensor types in terms of the error values could not be determined, which can be explained by the relatively strong aiding of the deformation variables **b** by the comparatively accurate strain gauges. This resulted in a convergence of the estimated deformation variables of both configurations towards the simulated values, as shown in Figure 11. Furthermore, the plot shows that an excitation of four involved unit deformations from Table 1 could be registered, showing frequency components of the corresponding eigenfrequencies. Although higher unit deformations have less impact on the total deflection, their estimation in time and frequency domain can give valuable insight into the structural behaviour.

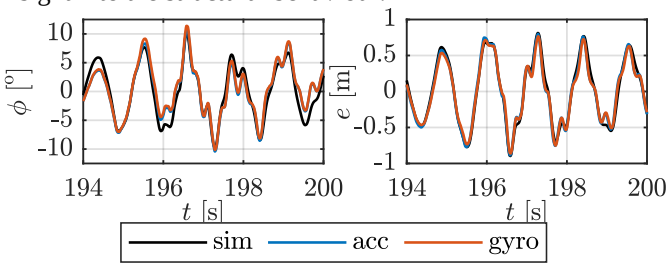

Figure 10. Attitude ϕ and pseudo-elastic deformation e with nearly identical results for “acc” and “gyro”.

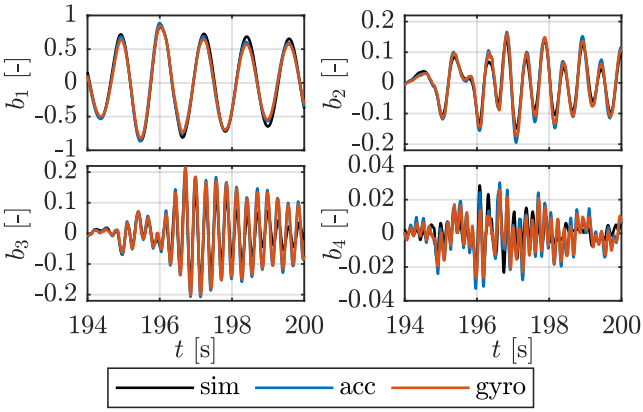

Figure 11. Deformation variables *b* [7].

For the scenario at hand a sample rate of 200 Hz of the IMUs and strain gauges turned out reasonable, whereas the distance measurements were sampled with 33.33 Hz due to technical limitations.

3.5 *Modal characteristics of deformation variables*

In addition to the conducted validation, the modal characteristics of the deformation variables are shortly investigated in this Subsection, following the state-of-the-art criteria in SHM from Section 1. For that, the single-sided amplitude spectrum of the deformation variables of the time interval from Figure 11 are plotted in Figure 12 for the “acc” and “gyro” configurations. To obtain the amplitude spectrum, the according signals are processed via FFT with a Hamming window and zero-padding to smooth the results. The eigenfrequencies of Table 1 are highlighted with red dotted lines, whereas the eigenfrequencies of the according unit deformations are marked with red dashed lines.

While all amplitudes show distinctive peaks at their according frequencies, a coupling of the different mode shapes is clearly seen, especially for the fourth unit deformation. This can be explained by the multiple nonlinearities of the system, like the Coulomb-Friction in the bearing [7]. Furthermore, the displacement function of Figure 9 has components of the fourth eigenfrequency during the analyzed time interval, which explains the strong coupling of the fourth deformation variable. To minimize the nonlinearities, the bearing was fixed in a

DOI: 10.3217/978-3-99161-057-1-070

purely simulative model, forcing the attitude $\phi = 0$ at all times. Subsequently, the sensor data were obtained by the FE simulation with the same input of Figure 9. For a short overview of the fundamental changes by the linearization of the system, the deformation variables b_3 and b_4 are plotted in Figure 13 for the same selected time interval. Due to the system changes, a combimode according to Figure 5 is no longer necessary. Therefore the deformation variables b_3 and b_4 of Figure 13 correspond to b_2 and b_3 of Figure 11.

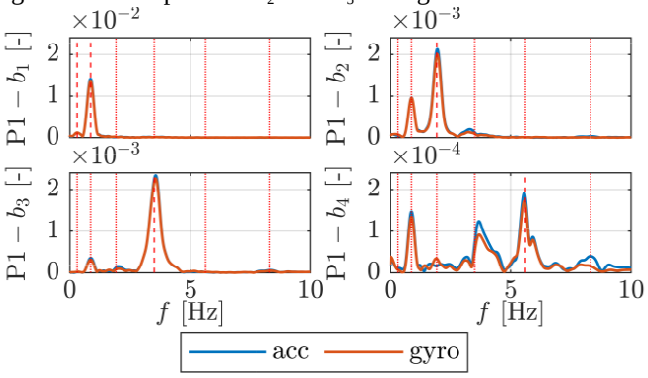

Figure 12. Single-sided amplitude spectrum of the deformation variables from Figure 11.

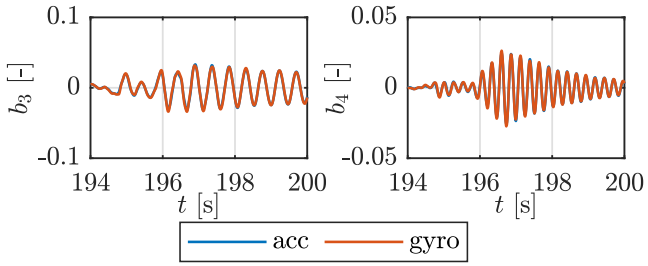

Figure 13. Deformation variables b_3 and b_4 for a simulated linearized system due to a fixed bearing ($\phi = 0$).

Analogously, the single sided amplitude spectrum with the adapted eigenfrequencies is shown in Figure 14. Figures 13 and 14 show that a decoupling of the included deformation variables can be observed. This indicates that if the unit deformations are set according to the mode shapes of the structure, the deformation variables reflect the associated modal parameters of natural frequencies and modal damping. The prerequisite for this is, however, that the system is linear or at least linear during certain time intervals.

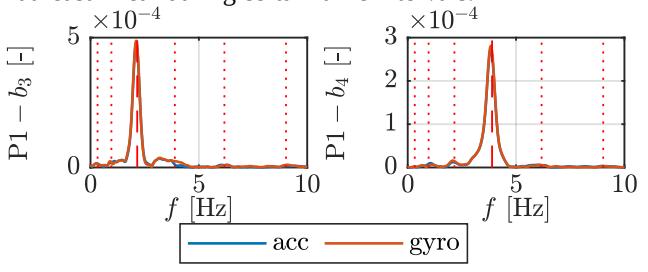

Figure 14. Single-sided amplitude spectrum of the deformation variables b_3 and b_4 from Figure 13.

4 EXPERIMENTAL APPROACH

This part of the study follows the experimental validation of IMMS [7], which was recapped in Section 3.4, to assess the importance of strain gauges. It is based on a pendulum equipped with 18 PCBs (holding IMUs and ToFs) and 12 strain gauge arrays (wheatstone full bridge), which were placed to investigate different configurations. According to each chosen sensor configuration, the optimal set of sensors is selected according to the method of Effective Independence [4,23] out of the available test beam. In analogy to the conducted validation, the system is excited by the displacement function of Figure 9. Furthermore, only configurations with four additional unit deformations $\Gamma = 4$ are investigated. Due to the similarity of the results from Figure 10 and 12, the configuration with four unit deformations and four peripheral gyroscopes, strain gauges and ToFs (gyro: $\nu_s = \nu_\rho = \nu_\varepsilon = 4$) serves as a new benchmark (bm) to compare and evaluate the acquired results. The comparative parameters are the attitude angle ϕ of the bearing, the pseudo-elastic deformation e, as well as the deformation variables $b_1, \ldots, b_4$. Of these, the error values are evaluated by calculating the root mean square error (RMSE) according to

$$\Delta x_{\text{rmse}} = \sqrt{\frac{1}{N}\sum_{i=1}^{N}(x_{\text{bm},i} - \hat{x}_i)^2} \tag{21}$$

for an arbitrary variable x with N samples. Again, the sample rate of the input vector and strain gauges (if used) is set to 200 Hz, while the ToFs and the linear distance sensor are set to 33.33 Hz as in Section 3.4.

To evaluate the importance of strain gauges, or more precisely the accurate aiding of the deformation variables in IMMS applications, the experimental procedure is divided into the following steps:

- Removing strain gauges:
  In the first step, an accelerometer and gyroscope configuration with four peripheral inertial sensors and ToFs (acc/gyro: $\nu_s = \nu_\rho = 4$, $\nu_\varepsilon = 0$) are compared against the benchmark.
- Extended aiding by redundant ToFs:
  To compensate for omitted strain gauges, configurations with varying number of peripheral ToFs $\nu_\rho = 4, \ldots, 13$ and redundant inertial sensors $\nu_s = 4,5$ are created.
- Aiding with reduced number of strain gauges:
  A reduced number of strain gauges $\nu_\varepsilon = 1,2,3$ are employed. Even though measurement Equation (19) becomes underdetermined in this case, aiding can still be employed via the EKF. Based on the preceding results, a reduced set of deformation variables $\mathbf{b}_{\varepsilon,\text{aided}}$ is aided by the strain gauges, leaving a remaining set of unaided deformation variables $\mathbf{b}_{\varepsilon,\text{unaided}}$. So, the strain gauges are selected in such a way that their placement is optimal with respect to $\mathbf{b}_{\varepsilon,\text{aided}}$. If the unaided deformation variables $\mathbf{b}_{\varepsilon,\text{unaided}}$ are already accurately estimated by e.g. redundant ToFs, their contribution to the bending strain can be subtracted from Equation (19). Accordingly, the matrix $\mathbf{S}''_\varepsilon$ is separated, resulting in the adapted aiding Equation

$$\boldsymbol{\varepsilon} - \mathbf{S}''_{\varepsilon,\text{unaided}} \cdot \mathbf{b}_{\varepsilon,\text{unaided}} = \mathbf{S}''_{\varepsilon,\text{aided}} \cdot \mathbf{b}_{\varepsilon,\text{aided}} = \mathbf{h}(\mathbf{b}_{\varepsilon,\text{aided}}). \tag{22}$$

Consequently, the left-hand side of Equation (22) is the adapted bending strain, associated to the aided deformation variables. The resulting configurations are supplemented by additional ToFs $\nu_\rho = 4, \ldots, 13$.

DOI: 10.3217/978-3-99161-057-1-070

Depending on the degree of observability and quality of aiding measurements, a careful filter tuning of the EKF can become a crucial task [24]. This applies especially to the cases of removed and reduced strain gauges. In these cases, the settings of the EKF are adapted in an appropriate range. However, by applying extensive filter tuning, the results can be further improved for any of the applied methods.

5 RESULTS

The results are presented in the order as they are introduced in Section 4. The configurations in the following subsections will be either with accelerometers (acc) or gyroscopes (gyro) as peripheral input sensors. If not specified otherwise, the number of peripheral sensors are set according to the case with removed strain gauges ($\nu_s = \nu_\rho = 4,\ \nu_\varepsilon = 0$).

5.1 Removing strain gauges

To demonstrate a general effect on the estimated system states by removing the direct aiding of the deformation variables, the estimates of attitude ϕ and pseudo-elastic deformation e are displayed on the left side of Figure 15 for the whole time interval of excitation.

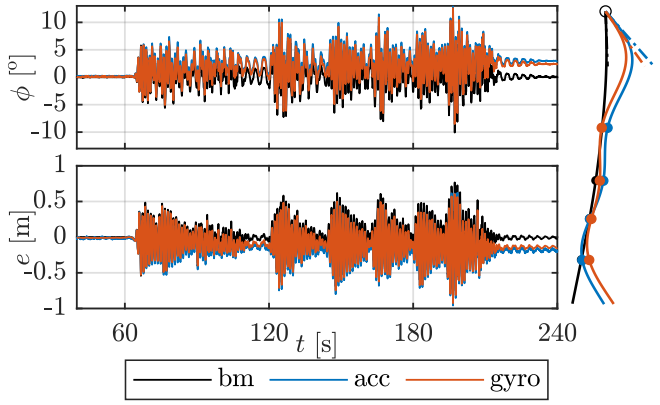

Figure 15. Estimated attitude ϕ and pseudo-elastic deformation e (left), and overscaled beam deformation at t = 230 s (right) for the acc and gyro configuration without strain gauges, compared to bm.

Both configurations show a gradual drift from the bm-values for both selected parameters in opposite directions, meaning that the attitude diverges contrary to the pseudo-elastic deformation. This behavior becomes apparent by visualizing the deformed, suspended beams at time $t = 230$ s on the right side of Figure 15. The graph displays the three configurations including the bearing D indicated by the black circle. The deformations of the beam are overscaled to emphasize the occurring effect. Additionally, the positions of the involved ToFs are marked by dots on the deformed structures. The tangent lines on the beam origin is plotted by dash-dotted lines, visualizing the attitude ϕ against an imaginary vertical line. Although the positions of the ToFs are accurate within the limits of their sensor error, the bending lines show a clear mismatch with respect to the benchmark. Without direct aiding of the elastic deformations and restricted accuracy of the ToFs, the aiding Equation (18) allows seemingly arbitrary combinations of ϕ and $\mathbf{b}$ to match the distance measurements. Ultimately, an overestimated attitude is compensated by an underestimated deformation.

In analogy to Figure 11, the deformation variables are plotted for the same time interval of high dynamics in Figure 16. The first deformation variable b_1 is estimated accurately. This can be explained by its comparatively high amplitude, which can be resolved by the distance measurements. The deformation variables b_2 to b_4 display the observed drift, however in phases of high amplitude the estimations are partially corrected towards the bm values (especially b_2 and b_3). Furthermore, the gyro configuration displays a smoother and qualitatively more accurate representation of the deformation variables than the acc configuration.

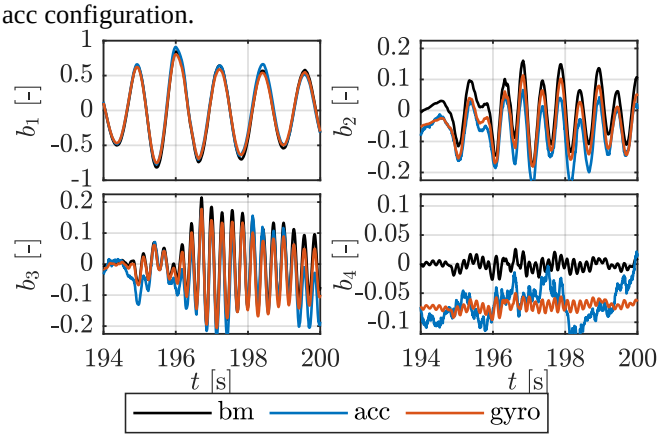

Figure 16. Estimated deformation variables b for the acc and gyro configurations without strain gauges, compared to bm.

5.2 Aiding by redundant ToFs

To compensate for the effects displayed in Figures 13 and 14, varying number of ToFs $\nu_\rho = 4,...,13$ are employed in combination with $\nu_s = 4,5$. The RMSE of ϕ and e according to Equation (21) is plotted in Figure 17 for the new acc and gyro configurations. With one additional ToF $\nu_\rho = 5$, both error values for both sensor types can be reduced significantly. By further increasing ν_ρ the errors can be further decreased, however both error values converge towards a limit. Redundant inertial sensors show no positive effect, which is why they will be dismissed for further evaluation.

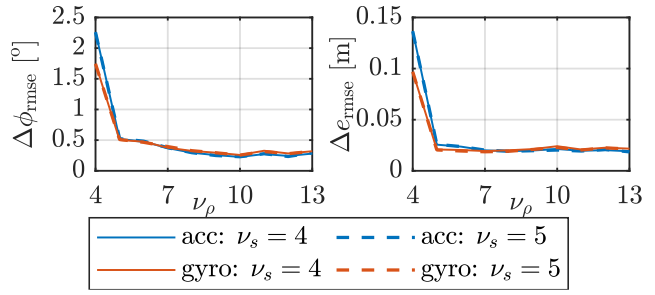

Figure 17. RMSE of the estimated attitude ϕ and pseudo-elastic deformation e for the acc and gyro configuration with additional ToFs, compared to bm.

To show the reduced drift, the attitude ϕ and pseudo-elastic deformation e for two exemplary acc and gyro configurations with $\nu_\rho = 10$ is plotted in Figure 18 for the respective time interval. All cases display a satisfactory estimate, with the unwanted drift significantly reduced.

Accordingly, the deformation variables are displayed in Figure 19, analogously to Figure 16. While still displaying a reduced deviation, b_2 to b_4 are no longer shifted exclusively in

DOI: 10.3217/978-3-99161-057-1-070

the negative direction. Again, the gyro configuration displays a superior behavior regarding the deformation variables.

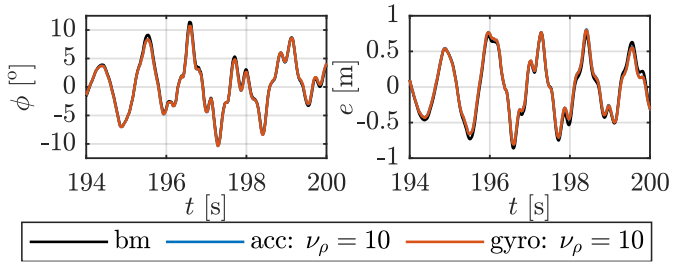

Figure 18. Attitude ϕ and pseudo-elastic deformation e for exemplary acc and gyro configurations with additional ToFs, compared to bm.

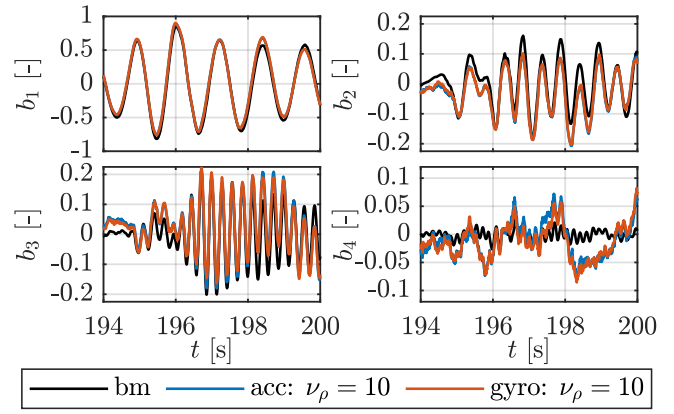

Figure 19. Estimated deformation variables b for the acc and gyro configurations with additional ToFs, compared to bm.

Overall, the negative effects of removing the direct aiding of the deformations can be significantly compensated (but not prevented by placing additional ToFs on the structure). This is because the aiding is carried out by Equation (18), which also involves deformation variables. However, the Equation is highly nonlinear, and the measurement accuracy and frequency are not sufficient to distinguish the low amplitudes of higher deformation variables. The higher accuracy of gyroscopes can be explained by the one-time integration of $\mathbf{b}$ according to Equation (10) in comparison to the double integration of $\ddot{\mathbf{b}}$ for accelerometers.

5.3 Aiding with reduced number of strain gauges

From Section 5.2 it becomes apparent that additional ToFs can not fully replace all removed strain gauges. However, it could be proven that the first deformation variable b_1 is sufficiently aided by a system without strain gauges. Building on that, configurations with $\nu_\varepsilon = 1,2,3$ are created with the following specifications of Equation (22):

- $\nu_\varepsilon = 1$: $\mathbf{b}_{\varepsilon,\text{aided}} = [b_2 \quad b_3 \quad b_4]^\mathrm{T}$,
- $\nu_\varepsilon = 2$: $\mathbf{b}_{\varepsilon,\text{aided}} = [b_3 \quad b_4]^\mathrm{T}$,
- $\nu_\varepsilon = 3$: $\mathbf{b}_{\varepsilon,\text{aided}} = [b_2 \quad b_3 \quad b_4]^\mathrm{T}$.

The selection is based on the observation that a set of aided variables equal to the number of the strain gauges used turned out to be beneficial. Nevertheless, aiding only one deformation variable was not feasible in the present setup.

In analogy to Figure 17, the RMSE of ϕ and e are plotted in Figure 20 including the comparative values of the gyro configuration $\nu_\rho = 10$ from the previous Section with a black, dash-dotted line. By employing at least one strain gauge, the errors are comparable or better to the one achieved with additional ToFs. By increasing their number, the errors can be further decreased. Regarding the attitude and pseudo-elastic deformation, the gyro configurations with $\nu_\varepsilon = 2$ displays a superior behavior.

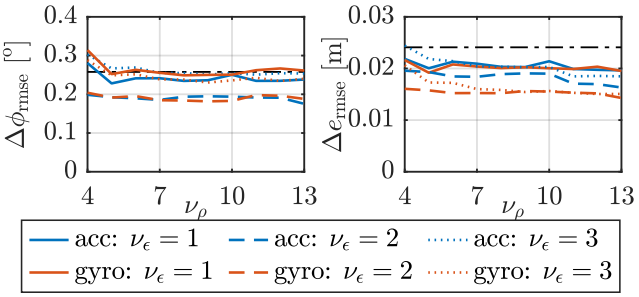

Figure 20. RMSE of the estimated attitude ϕ and pseudo-elastic deformation e for the acc and gyro configuration with reduced number of strain gauges, compared to bm.

Assuming an adequate estimation of b_1 and b_2 according to the previous Sections, the RMSEs of b_3 and b_4 are further assessed in Figure 21. The errors decrease with increasing number of strain gauges, whereas the gyro configurations show superior characteristics for each number of strain gauges.

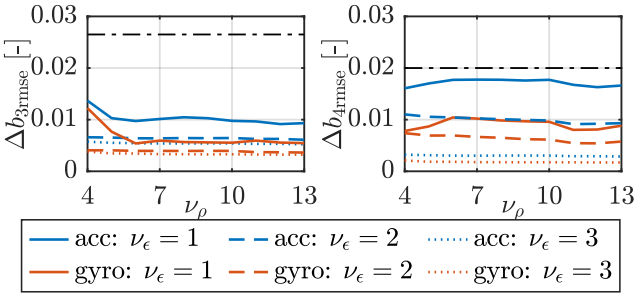

Figure 21. RMSE of the estimated deformation variables b_3 and b_4 for the acc and gyro configuration with reduced number of strain gauges, compared to bm.

The results suggest that a configuration with gyros and one strain gauge is comparable to accelerometers with two strain gauges and the same number of ToFs. Thus, the estimation of b_3 and b_4 for two corresponding configurations (acc: $\nu_\varepsilon = 2$, $\nu_\rho = 10$, gyro: $\nu_\varepsilon = 1$, $\nu_\rho = 10$) is plotted in Figure 22 for the selected time interval. Despite comparable RMSE values, the estimation of the gyro configuration approaches the bm values significantly better.

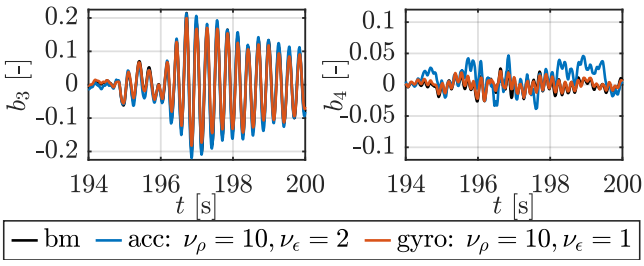

Figure 22. Estimated deformation variables b_3 and b_4 for the acc and gyro configurations with reduced number of strain gauges.

Concerning redundant ToFs and a reduced number of strain gauges, an attitude error of around $\Delta\phi \approx 0.3°$ corresponds to a

DOI: 10.3217/978-3-99161-057-1-070

deflection of roughly $\Delta e \approx 0.02\text{m}$, which matches the error values of Figures 15 and 18. This error is within the limit of accuracy of the measurements and modelling errors. The gain in accuracy of the deformation variables is the result of their direct aiding through Equation 22. Nevertheless, the attitude and total deflection can not be further improved. Although the error $\Delta b_{4,\text{rmse}}$ is roughly the same according to Figure 21 for the inspected case in Figure 22, the latter shows a superior performance of the gyro configuration. This can be achieved, even with fewer strain gauges than the accelerometer case.

6 CONCLUSIONS

In this study, IMMS are presented as a comprehensive tool for determining rigid and elastic movements of a wide range of possible structures. In addition to a general categorization within possible SHM applications, the reduction of high-maintenance sensors like strain gauges was investigated.

This study showed that the direct aiding of the deformation variables is crucial for a precise estimation of the state variables. It could be shown that redundant position aiding via distance sensors can not fully compensate for a loss of strain sensors, but the negative effects could be largely reduced. However, a reduction in strain gauges is feasible without an essential loss in accuracy. This can be achieved by aiding larger deformations with the available distance sensors and small deformations by the accurate remaining strain gauges.

With respect to the deformation variables, it could be shown that modal parameters are represented within the time and frequency domain. Even for a nonlinear system, the deformation variables show distinctive frequency peaks at their corresponding eigenfrequencies of the linearization. A linear simulated system holds the potential to estimate the modal amplitudes in the time domain during operation. With current SHM approaches using modal parameters like eigenfrequencies, mode shapes, or damping ratios, the estimation of the deformation variables in time and frequency domain are potential parameters to be analyzed. Eigenfrequencies could thus be extracted from the frequency, while the modal damping ratio could be extracted from the time domain. Both time and frequency domain of the deformation variables could also serve as an input for Finite Element Model Updating to localize simulated damage mechanisms. Additionally, the estimated deformation and curvature of the structure can indicate changes in the mode shapes due to damage. Furthermore, the precise movement analysis can give insight into loads and strains during operation and can therefore be included in the estimation of the remaining service life. In conclusion, this study could show the existing potential of IMMS for SHM.

Next steps will apply artificial “damages” in the form of additional masses or stiffeners to the test beam. Subsequently, the influence of these structural changes on the behavior of the deformation variables in time and frequency domain will be analyzed according to the presented state-of-the-art methods in SHM. Further steps could replicate the linearized system with a fixed bearing and a sensitivity analysis regarding sensor requirements like accuracy and noise in combination with quantity. Ultimately, the benefit of IMMS in relation to state-of-the-art methods needs to be proven experimentally.

REFERENCES

[1] J. A. Farrell and M. J. Barth, The Global Positioning System and Inertial Navigation, McGraw-Hill, New York, USA, 1999.
[2] D. Titterton and J. L. Weston, Strapdown Inertial Navigation Technology, IET, Stevenage, UK, second edition 2004.
[3] J. F. Wagner and G. Kasties, Improving the GPS/INS Integrated System Performance by Increasing the Distance Between GPS Antennas and Inertial Sensors, Proc. 2002 Nat. Tech. Meeting Inst. Navigation, pp. 103-115, Jan. 2002.
[4] T. Örtel, Integrierte Bewegungsmessung an flexiblen Strukturen. Dr. Hut, München, Germany, 2010.
[5] M. Kohl et al., Test Rig for Validating the Integrated Motion Measurement of Flexible Beam, Proc. Appl. Math. Mechan., vol. 24, no. 4, pp. 1-11, 2024, doi: 10.1002/pamm.202400061.
[6] J. F. Wagner et al., Hybrid Sensor System for Integrated Structural Motion Measurement, IEEE Sensors Letters, vol. 9, no. 3, pp. 1-4, March 2025, doi: 10.1109/LSENS.2025.3540358.
[7] M. Kohl and J. F. Wagner, Validating the Integrated Motion Measurement of Flexible Beams, 2024 DGON Inertial Sensors and Applications, pp. 1-21, 2024, doi: 10.1109/ISA62769.2024.10786046.
[8] S. Keil, Dehnungsmessstreifen, Springer, Wiesbaden, Germany, second edition, 2017.
[9] C. P. Fritzen, Vibration-Based Structural Health Monitoring – Concepts and Applications, Key Engineering Materials, vol. 293-294, pp. 3-20, Sept. 2005, doi: 10.4028/www.scientific.net/kem.293-294.3.
[10] D. Goyal and B. S. Pable, The Vibration Monitoring Methods and Signal Processing Techniques for Structural Health Monitoring: A Review, Arch. Comput. Methods Eng., vol. 23, pp. 585-594, 2016, doi: 10.1007/s11831-015-9145-0.
[11] W. Dai et al., DAI, Multi-Antenna Global Navigation Satellite System/Inertial Measurement Unit Tight Integration for Measuring Displacement and Vibration in Structural Health Monitoring, Remote Sensing, vol. 16, no. 6, p. 1072, doi: 10.3390/rs16061072.
[12] N. Shen et al., Multi-route fusion method of GNSS and accelerometer for structural health monitoring, J. Ind. Inf. Integr., vol. 32, p. 100442, 2023, doi: 10.1016/j.jii.2023.100442.
[13] X. Qu et al., Real-time outlier detection in integrated GNSS and accelerometer structural health monitoring systems based on a robust multi-rate Kalman filter, J. Geod., vol. 97, no. 4, p. 38, 2023, doi: 10.1007/s00190-023-01724-2.
[14] M. Omidalizarandi et al., A validated robust and automatic procedure for vibration analysis of bridge structures using MEMS accelerometers, J. Appl. Geod., vol. 14,no. 3, pp. 327-354,2020, doi: 10.1515/jag-2020-0010.
[15] A. R. Al-Ali et al., An IoT-Based Road Bridge Health Monitoring and Warning System, Sensors, vol. 24, no. 2, p. 469, 2024, doi: 10.3390/s24020469.
[16] A. M. Cooperman and M. J. Martinez, MEMS for structural health monitoring of wind turbine blades, 25th International Conference on Adaptive Structures and Technologies, pp. 1-6, 2024.
[17] G. Faraco et al., Structural Health Monitoring by Accelerometric Data of a Continuously Monitored Structure with Induced Damages, Structural Durability & Health Monitoring (SDHM), vol. 18, no. 6, pp. 739-762, 2024, doi: 10.32604/sdhm.2024.052663.
[18] H. C. Kim et al., Structural health monitoring of towers and blades for floating offshore wind turbines using operational modal analysis and modal properties with numerical-sensor signals, Ocean Engineering, vol. 188, p. 106226, 2019, doi: 10.1016/j.oceaneng.2019.106226.
[19] J. Pacheco-Cherrez et al., Operational modal analysis for damage detection in a rotating wind turbine blade in the presence of measurement noise, Composite Structures, vol. 321, p. 117298, 2023, doi: 10.1016/j.compstruct.2023.117298.
[20] T. J. Arsenault et al., Development of a FBG based distributed strain sensor system for wind turbine structural health monitoring, Smart Materials and Structures, vol. 22, no. 7, p. 075027, 2013, doi: 10.1088/0964-1726/22/7/075027.
[21] A. Haidarpour and F. T. Kong, Finite Element Model Updating for Structural Health Monitoring, Structural Durability & Health Monitoring, vol. 14, no. 1, pp. 1-17, 2020, doi: 10.32604/sdhm.2020.08792.
[22] J. F. Wagner and T. Wieneke, Integrating Satellite and Inertial Navigation—Conventional and New Fusion Approaches, Control Eng. Pract., vol. 11, no. 5, pp.543-550, May 2003, doi: 10.1016/S0967- 0661(02)00043-6.
[23] D. C. Kammer, Sensor Placement for On-Orbit Modal Identification and Correlation of Large Space Structures, J. Guid., Control, Dyn., 1991, vol. 14, no. 2, pp. 251-259, doi: 10.2514/3.20635.
[24] J. F. Wagner et al., Reevaluation of Algorithmic Basics for ZUPT-Based Pedestrian Navigation, IEEE Access, vol. 10, pp. 118419–118437, 2022, doi: 10.1109/ACCESS.2022.3220629.